Available online at www.sciencedirect.com
ScienceDirect
International Journal of Thermal Sciences 47 (2008) 7–24
International Journal of Thermal Sciences
www.elsevier.com/locate/ijts

A finite difference method for studying thermal deformation in a double-layered thin film with imperfect interfacial contact exposed to ultrashort pulsed lasers

Haojie Wang [a], Weizhong Dai [a,*], Lionel G. Hewavitharana [b]

[a] *Mathematics & Statistics, College of Engineering & Science, Louisiana Tech University, Ruston, LA 71272, USA*
[b] *Mechanical Engineering, College of Engineering & Science, Louisiana Tech University, Ruston, LA 71272, USA*

Received 2 August 2006; received in revised form 15 January 2007; accepted 15 January 2007

Available online 26 February 2007

Abstract

Recently, we have developed a staggered finite difference method for studying thermal deformation in a two-dimensional double-layered metal film exposed to ultrashort pulsed lasers. The method was obtained based on the parabolic two-step heat transport equations. It accounts for the coupling effect between lattice temperature and strain rate, as well as for the hot-electron blast effect in momentum transfer. The developed methodology allows us to avoid non-physical oscillations in the solution as demonstrated by a series of numerical experiments. In this article, we extend our research to the case that the double-layered thin film is imperfect thermal contact at interface. Nonlinear interfacial condition for temperature is considered. The interfacial conditions for stress, strain, and displacement are derived.

Keywords: Ultrashort-pulsed lasers; Thermal deformation; Finite difference method; Double-layered thin film; Staggered grid; Two-step model; Imperfect interfacial contact

1. Introduction

Ultrafast lasers with pulse durations of the order of subpicoseconds to femtoseconds possess exclusive capabilities in limiting the undesirable spread of the thermal process zone in the heated sample [1]. The application of ultrashort-pulsed lasers includes structural monitoring of thin metal films [2, 3], laser micromachining [4] and patterning [5], structural tailoring of microfilms [6], and laser synthesis and processing in thin-film deposition [7]. Recent applications of ultrashort-pulsed lasers have been in different disciplines such as physics, chemistry, biology, medicine, and optical technology [8–14]. The non-contact nature of femtosecond lasers has made them an ideal candidate for precise thermal processing of functional nanophase materials [1].

Up to date, as we know, a mathematical model has been developed by Tzou and his colleagues [1] for studying thermal deformation in a double-layered thin film exposed to ultrashort pulsed lasers. They presented a one-dimensional model in a double-layered thin film. The model was solved using a differential-difference approach. Recently, we have presented a two-dimensional plain strain thin film model in rectangular coordinates [15,16]. The film is exposed to ultrashort pulsed lasers. An implicit finite difference scheme on a staggered grid for studying thermal deformation induced by ultrashort pulsed lasers is developed based on the parabolic two-step heat transport equations. It accounts for the coupling effect between lattice temperature and strain rate, as well as for the hot-electron blast effect in momentum transfer. The developed methodology allows us to avoid non-physical oscillations in the solution as demonstrated by a series of numerical experiments. In this article, we extend our research to the case that the double-layered thin film is imperfect thermal contact at interface. The extended research is helpful for studying the effects of acoustic and diffuse phonon mismatch across the interface, because such as effect will generate additional nonlinear behavior in the interfacial area [17–19].

* Corresponding author.
E-mail address: dai@coes.latech.edu (W. Dai).

1290-0729/$ – see front matter
doi:10.1016/j.ijthermalsci.2007.01.023

Nomenclature

C_{e0}	electron heat capacity	$\mathrm{J\,m^{-3}K^{-1}}$
C_l	lattice heat capacity	$\mathrm{J\,m^{-3}\,K^{-1}}$
E	Young's module	Pa
G	electron-lattice coupling factor	$\mathrm{W\,m^{-3}\,K^{-1}}$
J	laser fluence	$\mathrm{J\,m^{-2}}$
k_e	thermal conductivity	$\mathrm{W\,m^{-1}\,K^{-1}}$
m	layer	
R	surface reflectivity	
T_e	electron temperature	K
T_l	lattice temperature	K
t, t_n	time	s
t_p	laser pulse duration	s
u, v	displacements in x and y directions, respectively	m
u_{ij}^n	numerical solution of $u(x_i, y_j, t_n)$	m
v_1, v_2	velocity components in x and y directions, respectively	$\mathrm{m\,s^{-1}}$
x, y	Cartesian coordinates	
x_s	optical penetration depth	m
y_s	spatial profile parameter	m
α_T	thermal expansion coefficient	$\mathrm{K^{-1}}$
$\Delta t, \Delta x, \Delta y$	time increment and spatial step sizes, respectively	s, m, m

Greek symbols

$\Delta_{-t}, \delta_x, \delta_y$	finite difference operators	
$\varepsilon_x, \varepsilon_y$	normal strains in x and y directions, respectively	
Λ	electron-blast coefficient	$\mathrm{J\,m^{-3}\,K^{-2}}$
γ_{xy}	shear strain	
λ	Lame's coefficient	Pa
μ	Lame's coefficient	Pa
E	modulus of elasticity	Pa
ρ	density	$\mathrm{kg\,m^{-3}}$
σ	Boltzman's constant	$\mathrm{W\,m^{-2}\,K^{-4}}$
σ_x, σ_y	normal stresses in x and y directions, respectively	Pa
σ_{xy}	Shear stress	Pa

2. Mathematical model

Consider a two-dimensional double-layered thin film in rectangular coordinates, which is exposed to ultrashort pulsed lasers, as shown in Fig. 1. The governing equations for studying thermal deformation in the thin film can be expressed as follows:

(1) *Dynamic equations of motion* [1,20,21]

$$\rho^{(m)}\frac{\partial^2 u^{(m)}}{\partial t^2} = \frac{\partial \sigma_x^{(m)}}{\partial x} + \frac{\partial \sigma_{xy}^{(m)}}{\partial y} + 2\Lambda^{(m)} T_e^{(m)}\frac{\partial T_e^{(m)}}{\partial x} \tag{1}$$

$$\rho^{(m)}\frac{\partial^2 v^{(m)}}{\partial t^2} = \frac{\partial \sigma_{xy}^{(m)}}{\partial x} + \frac{\partial \sigma_y^{(m)}}{\partial y} + 2\Lambda^{(m)} T_e^{(m)}\frac{\partial T_e^{(m)}}{\partial y} \tag{2}$$

where

$$\varepsilon_x^{(m)} = \frac{\partial u^{(m)}}{\partial x}, \qquad \varepsilon_y^{(m)} = \frac{\partial v^{(m)}}{\partial y}$$

$$\gamma_{xy}^{(m)} = \frac{\partial u^{(m)}}{\partial y} + \frac{\partial v^{(m)}}{\partial x} \tag{3}$$

$$\sigma_x^{(m)} = \lambda^{(m)}\left(\varepsilon_x^{(m)} + \varepsilon_y^{(m)}\right) + 2\mu^{(m)}\varepsilon_x^{(m)} - \left(3\lambda^{(m)} + 2\mu^{(m)}\right)\alpha_T^{(m)}\left(T_l^{(m)} - T_0\right) \tag{4}$$

$$\sigma_y^{(m)} = \lambda^{(m)}\left(\varepsilon_x^{(m)} + \varepsilon_y^{(m)}\right) + 2\mu^{(m)}\varepsilon_y^{(m)} - \left(3\lambda^{(m)} + 2\mu^{(m)}\right)\alpha_T^{(m)}\left(T_l^{(m)} - T_0\right) \tag{5}$$

$$\sigma_{xy}^{(m)} = \mu^{(m)}\gamma_{xy}^{(m)} \tag{6}$$

Here, $m = 1, 2$, denotes layer 1 and layer 2, respectively; $u^{(m)}$ is the displacement in the thickness direction (x-direction) and $v^{(m)}$ is the displacement in the length direction (y-direction); $\varepsilon_x^{(m)}$ and $\varepsilon_y^{(m)}$ are the normal strains in x and y directions, respectively; $\gamma_{xy}^{(m)}$ is the shear strain; $\sigma_x^{(m)}$ and $\sigma_y^{(m)}$ are the normal stresses in x and y directions, respectively; $\sigma_{xy}^{(m)}$ is the shear stress; $T_e^{(m)}$ and $T_l^{(m)}$ are electron and lattice temperatures, respectively; T_0 is the initial temperature; $\rho^{(m)}$ is density; $\Lambda^{(m)}$ is electron-blast coefficient; $\lambda^{(m)}$ and $\mu^{(m)}$ are Lame's coefficients; and $\alpha_T^{(m)}$ is thermal expansion coefficient.

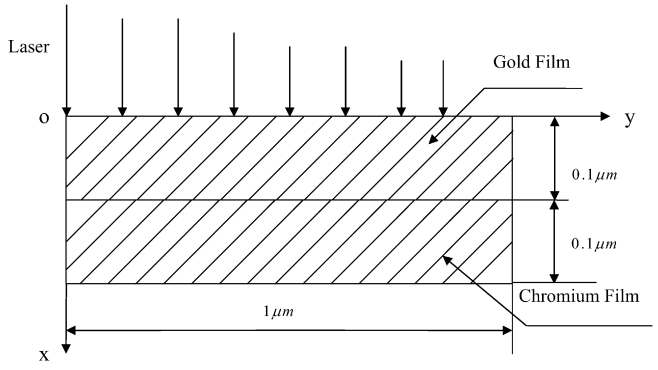

Fig. 1. Laser heating model.

(2) *Energy equations* [1,21,22]

$$\left(C_e(T_e)\right)^{(m)}\frac{\partial T_e^{(m)}}{\partial t} = \frac{\partial}{\partial x}\left[\left(k_e(T_e, T_l)\right)^{(m)}\frac{\partial T_e^{(m)}}{\partial x}\right] + \frac{\partial}{\partial y}\left[\left(k_e(T_e, T_l)\right)^{(m)}\frac{\partial T_e^{(m)}}{\partial y}\right] - G^{(m)}\left(T_e^{(m)} - T_l^{(m)}\right) + Q \tag{7}$$

$$C_l^{(m)}\frac{\partial T_l^{(m)}}{\partial t} = G^{(m)}\left(T_e^{(m)} - T_l^{(m)}\right) - \left(3\lambda^{(m)} + 2\mu^{(m)}\right)\alpha_T^{(m)}\frac{\partial}{\partial t}\left(\varepsilon_x^{(m)} + \varepsilon_y^{(m)}\right) \tag{8}$$

where the heat source is given by

$$Q = 0.94J\frac{1-R}{t_p x_s}\exp\left[-\frac{x}{x_s}-\left(\frac{y}{y_s}\right)^2-2.77\left(\frac{t-2t_p}{t_p}\right)^2\right] \quad (9)$$

Here, $(C_e(T_e))^{(m)} = C_{e0}^{(m)}\cdot\frac{T_e^{(m)}}{T_0}$ is the electron heat capacity; $(k_e(T_e,T_l))^{(m)} = k_{e0}^{(m)}\cdot\frac{T_e^{(m)}}{T_l^{(m)}}$ is the electron thermal conductivity; $G^{(m)}$ is the electron-lattice coupling factor; $C_l^{(m)}$ is the lattice heat capacity; Q is energy absorption rate; J is laser fluence; R is surface reflectivity; t_p is laser pulse duration; x_s is optical penetration depth, and y_s is spatial profile parameter. Eqs. (7) and (8) are often referred to as parabolic two-step heat transport equations.

(3) *Interfacial conditions*

The nonlinear interfacial condition for T_e can be written as follows [17–19]:

$$-k_e^{(1)}\frac{\partial T_e^{(1)}}{\partial x} = -k_e^{(2)}\frac{\partial T_e^{(2)}}{\partial x} = \sigma\left[\left(T_e^{(1)}\right)^4-\left(T_e^{(2)}\right)^4\right]$$
$$T_e^{(1)} \neq T_e^{(2)} \quad (10)$$

where $\sigma = 5.669\times10^{-8}\ \mathrm{W\,m^{-2}\,K^{-4}}$ is Boltzman's constant. Once T_e is obtained, T_l at interface can be obtained based on Eq. (8).

To obtain the interfacial conditions for stress and displacement, we first assume that shear stresses are equal at interface,

$$\sigma_{xy}^{(1)} = \sigma_{xy}^{(2)} \quad (11)$$

From Eqs. (3) and (6), we obtain that $\mu^{(1)}\gamma_{xy}^{(1)} = \mu^{(2)}\gamma_{xy}^{(2)}$ and hence $\mu^{(1)}(\frac{\partial u^{(1)}}{\partial y}+\frac{\partial v^{(1)}}{\partial x}) = \mu^{(2)}(\frac{\partial u^{(2)}}{\partial y}+\frac{\partial v^{(2)}}{\partial x})$. It is noted that if $\mu^{(1)}\frac{\partial u^{(1)}}{\partial y} = \mu^{(2)}\frac{\partial u^{(2)}}{\partial y}$ and $\mu^{(1)}\frac{\partial v^{(1)}}{\partial x} = \mu^{(2)}\frac{\partial v^{(2)}}{\partial x}$, then $\mu^{(1)}(\frac{\partial u^{(1)}}{\partial y}+\frac{\partial v^{(1)}}{\partial x}) = \mu^{(2)}(\frac{\partial u^{(2)}}{\partial y}+\frac{\partial v^{(2)}}{\partial x})$ is satisfied. For the purpose of simple computation later on, we assume that $\mu^{(1)}\frac{\partial u^{(1)}}{\partial y} = \mu^{(2)}\frac{\partial u^{(2)}}{\partial y}$ and $\mu^{(1)}\frac{\partial v^{(1)}}{\partial x} = \mu^{(2)}\frac{\partial v^{(2)}}{\partial x}$. This leads us to assume the interfacial condition for displacements to be, for simplicity,

$$\mu^{(1)}u^{(1)} = \mu^{(2)}u^{(2)} \quad \text{and} \quad \mu^{(1)}v^{(1)} = \mu^{(2)}v^{(2)} \quad (12)$$

Based on this assumption, we obtain that $\mu^{(1)}(\frac{\partial u^{(1)}}{\partial x}) = \mu^{(2)}(\frac{\partial u^{(2)}}{\partial x})$ and hence $\mu^{(1)}\varepsilon_x^{(1)} = \mu^{(2)}\varepsilon_x^{(2)}$ from Eq. (3). Since, $\varepsilon_x^{(m)} = \frac{\sigma_x^{(m)}}{E^{(m)}} - \frac{\gamma^{(m)}\sigma_y^{(m)}}{E^{(m)}}$ [23], where E is Young's module and γ is Poisson ratio, we substitute it into $\mu^{(1)}\varepsilon_x^{(1)} = \mu^{(2)}\varepsilon_x^{(2)}$ and obtain $\mu^{(1)}(\frac{\sigma_x^{(1)}}{E^{(1)}} - \frac{\gamma^{(1)}\sigma_y^{(1)}}{E^{(1)}}) = \mu^{(2)}(\frac{\sigma_x^{(2)}}{E^{(2)}} - \frac{\gamma^{(2)}\sigma_y^{(2)}}{E^{(2)}})$. Again, for simplicity, we assume the interfacial condition for stress to be

$$\mu^{(1)}\left(\frac{\sigma_x^{(1)}}{E^{(1)}}\right) = \mu^{(2)}\left(\frac{\sigma_x^{(2)}}{E^{(2)}}\right) \quad (13)$$

Using a same argument as that in [15], the boundary conditions are assumed to be

$$\sigma_x^{(1)} = 0, \quad \sigma_{xy}^{(1)} = 0 \quad \text{at } x = 0, \quad \text{and}$$
$$\sigma_x^{(2)} = 0, \quad \sigma_{xy}^{(2)} = 0 \quad \text{at } x = L_x \quad (14)$$
$$\sigma_y^{(1)} = 0, \quad \sigma_{xy}^{(1)} = 0 \quad \text{at } y = 0, \quad \text{and}$$
$$\sigma_y^{(2)} = 0, \quad \sigma_{xy}^{(2)} = 0 \quad \text{at } y = L_y \quad (15)$$
$$\frac{\partial T_e^{(m)}}{\partial \vec{n}} = 0, \qquad \frac{\partial T_l^{(m)}}{\partial \vec{n}} = 0 \quad (16)$$

where $\vec{n}$ is the unit outward normal vector on the boundary.

The initial conditions are assumed to be

$$T_e^{(m)} = T_l^{(m)} = T_0, \qquad u^{(m)} = v^{(m)} = 0$$
$$u_t^{(m)} = v_t^{(m)} = 0, \quad \text{at } t = 0 \quad (17)$$

where $m = 1, 2$.

3. Finite difference method

Using a similar argument as that in [15], we introduce two velocity components $v_1^{(m)}$ and $v_2^{(m)}$ into the model and re-write the dynamic equations of motion, Eqs. (1)–(6), and the interfacial condition, Eq. (12), as follows:

$$v_1^{(m)} = \frac{\partial u^{(m)}}{\partial t}, \qquad v_2^{(m)} = \frac{\partial v^{(m)}}{\partial t} \quad (18)$$
$$\frac{\partial \varepsilon_x^{(m)}}{\partial t} = \frac{\partial v_1^{(m)}}{\partial x}, \qquad \frac{\partial \varepsilon_y^{(m)}}{\partial t} = \frac{\partial v_2^{(m)}}{\partial y}$$
$$\frac{\partial \gamma_{xy}^{(m)}}{\partial t} = \frac{\partial v_2^{(m)}}{\partial x} + \frac{\partial v_1^{(m)}}{\partial y} \quad (19)$$
$$\rho^{(m)}\frac{\partial v_1^{(m)}}{\partial t} = \frac{\partial \sigma_x^{(m)}}{\partial x} + \frac{\partial \sigma_{xy}^{(m)}}{\partial y} + \Lambda^{(m)}\frac{\partial (T_e^2)^{(m)}}{\partial x} \quad (20)$$
$$\rho^{(m)}\frac{\partial v_2^{(m)}}{\partial t} = \frac{\partial \sigma_{xy}^{(m)}}{\partial x} + \frac{\partial \sigma_y^{(m)}}{\partial y} + \Lambda^{(m)}\frac{\partial (T_e^2)^{(m)}}{\partial y} \quad (21)$$
$$\mu^{(1)}v_1^{(1)} = \mu^{(2)}v_1^{(2)}, \qquad \mu^{(1)}v_2^{(1)} = \mu^{(2)}v_2^{(2)} \quad (22)$$

To develop a finite difference scheme, we first construct a staggered grid as shown in Fig. 2, where $v_1^{(m)}$ is placed at $(x_{i+1/2}, y_j)$, $v_2^{(m)}$ is placed at $(x_i, y_{j+1/2})$, $\gamma_{xy}^{(m)}$ and $\sigma_{xy}^{(m)}$ are placed at $(x_{i+1/2}, y_{j+1/2})$, while $\varepsilon_x^{(m)}$, $\varepsilon_y^{(m)}$, $\sigma_x^{(m)}$, $\sigma_y^{(m)}$, $T_e^{(m)}$ and $T_l^{(m)}$ are at (x_i, y_j). Here, i and j are indices with $1 \leqslant i \leqslant N+1$ and $1 \leqslant j \leqslant M+1$. We denote $(v_1^n(i+1/2, j))^{(m)}$ and $(v_2^n(i, j+1/2))^{(m)}$ as numerical approximations of $v_1^{(m)}((i+1/2)\Delta x, j\Delta y, n\Delta t)$ and $v_2^{(m)}(i\Delta x, (j+1/2)\Delta y, n\Delta t)$, respectively, where $\Delta t, \Delta x$ and Δy are time increment and spatial step sizes, respectively. Similar notations are used for other variables. Furthermore, we introduce the finite difference operators, Δ_{-t} and δ_x as follows:

$$\Delta_{-t}u^n(i,j) = u^n(i,j) - u^{n-1}(i,j)$$
$$\delta_x u^n(i,j) = u^n(i+1/2,j) - u^n(i-1/2,j)$$
$$\delta_y u^n(i,j) = u^n(i,j+1/2) - u^n(i,j-1/2)$$

The finite difference method for solving the above governing equations are the same as those developed in [15] except for the interfacial conditions:

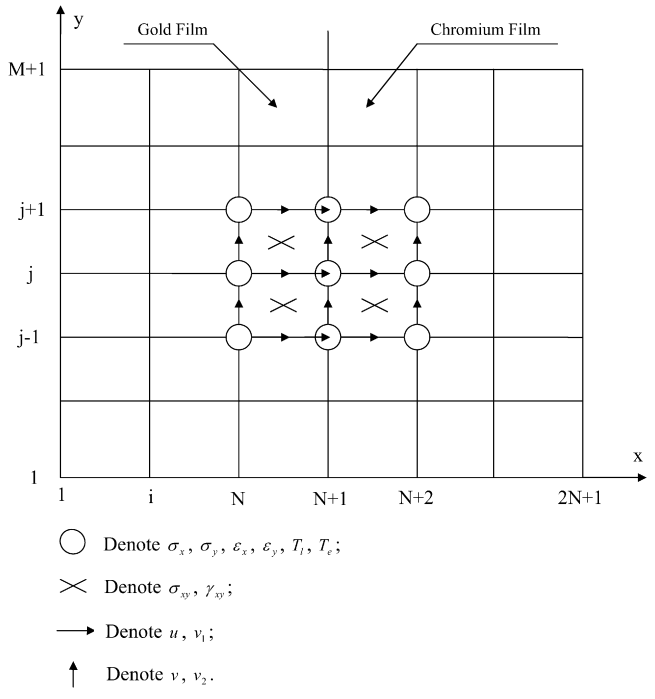

Fig. 2. A staggered mesh.

$$\rho^{(m)}\frac{1}{\Delta t}\Delta_{-t}\left(v_1^{n+1}\right)^{(m)}(i+1/2,\,j) = \frac{1}{\Delta x}\delta_x\left(\sigma_x^{n+1}\right)^{(m)}(i+1/2,\,j) + \frac{1}{\Delta y}\delta_y\left(\sigma_{xy}^{n+1}\right)^{(m)}(i+1/2,\,j) + \Lambda^{(m)}\frac{1}{\Delta x}\delta_x\left[\left(T_e^2\right)^{n+1}\right]^{(m)}(i+1/2,\,j) \tag{23}$$

$$\rho^{(m)}\frac{1}{\Delta t}\Delta_{-t}\left(v_2^{n+1}\right)^{(m)}(i,\,j+1/2) = \frac{1}{\Delta x}\delta_x\left(\sigma_{xy}^{n+1}\right)^{(m)}(i,\,j+1/2) + \frac{1}{\Delta y}\delta_y\left(\sigma_y^{n+1}\right)^{(m)}(i,\,j+1/2) + \Lambda^{(m)}\frac{1}{\Delta y}\delta_y\left[\left(T_e^2\right)^{n+1}\right]^{(m)}(i,\,j+1/2) \tag{24}$$

$$\frac{1}{\Delta t}\Delta_{-t}\left(\varepsilon_x^{n+1}\right)^{(m)}(i,\,j) = \frac{1}{\Delta x}\delta_x\left(v_1^{n+1}\right)^{(m)}(i,\,j) \tag{25}$$

$$\frac{1}{\Delta t}\Delta_{-t}\left(\varepsilon_y^{n+1}\right)^{(m)}(i,\,j) = \frac{1}{\Delta y}\delta_y\left(v_2^{n+1}\right)^{(m)}(i,\,j) \tag{26}$$

$$\frac{1}{\Delta t}\Delta_{-t}\left(\gamma_{xy}^{n+1}\right)^{(m)}(i+1/2,\,j+1/2) = \frac{1}{\Delta x}\delta_x\left(v_2^{n+1}\right)^{(m)}(i+1/2,\,j+1/2) + \frac{1}{\Delta y}\delta_y\left(v_1^{n+1}\right)^{(m)}(i+1/2,\,j+1/2) \tag{27}$$

$$\begin{aligned}\left(\sigma_x^{n+1}\right)^{(m)}(i,\,j) &= \lambda^{(m)}\left[\left(\varepsilon_x^{n+1}\right)^{(m)}(i,\,j)+\left(\varepsilon_y^{n+1}\right)^{(m)}(i,\,j)\right] + 2\mu^{(m)}\left(\varepsilon_x^{n+1}\right)^{(m)}(i,\,j) - \left(3\lambda^{(m)}+2\mu^{(m)}\right)\alpha_T^{(m)} \times\left[\left(T_l^{n+1}\right)^{(m)}(i,\,j)-T_0\right]\end{aligned} \tag{28}$$

$$\begin{aligned}\left(\sigma_y^{n+1}\right)^{(m)}(i,\,j) &= \lambda^{(m)}\left[\left(\varepsilon_x^{n+1}\right)^{(m)}(i,\,j)+\left(\varepsilon_y^{n+1}\right)^{(m)}(i,\,j)\right] + 2\mu^{(m)}\left(\varepsilon_y^{n+1}\right)^{(m)}(i,\,j) - \left(3\lambda^{(m)}+2\mu^{(m)}\right)\alpha_T^{(m)} \times\left[\left(T_l^{n+1}\right)^{(m)}(i,\,j)-T_0\right]\end{aligned} \tag{29}$$

$$\left(\sigma_{xy}^{n+1}\right)^{(m)}(i+1/2,\,j+1/2) = \mu^{(m)}\left[\left(\gamma_{xy}^{n+1}\right)^{(m)}(i+1/2,\,j+1/2)\right] \tag{30}$$

$$\begin{aligned}C_{e0}^{(m)}\frac{(T_e^{n+1})^{(m)}(i,\,j)+(T_e^{n})^{(m)}(i,\,j)}{2T_0}\frac{1}{\Delta t}\Delta_{-t}\left(T_e^{n+1}\right)^{(m)}(i,\,j) &= \frac{1}{2\Delta x^2}\left[\left(k_e^{n+1}\right)^{(m)}(i+1/2,\,j)\delta_x\left(T_e^{n+1}\right)^{(m)}(i+1/2,\,j) - \left(k_e^{n+1}\right)^{(m)}(i-1/2,\,j)\delta_x\left(T_e^{n+1}\right)^{(m)}(i-1/2,\,j)\right] \\ &+ \frac{1}{2\Delta x^2}\left[\left(k_e^{n}\right)^{(m)}(i+1/2,\,j)\delta_x\left(T_e^{n}\right)^{(m)}(i+1/2,\,j) - \left(k_e^{n}\right)^{(m)}(i-1/2,\,j)\delta_x\left(T_e^{n}\right)^{(m)}(i-1/2,\,j)\right] \\ &+ \frac{1}{2\Delta y^2}\left[\left(k_e^{n+1}\right)^{(m)}(i,\,j+1/2)\delta_y\left(T_e^{n+1}\right)^{(m)}(i,\,j+1/2) - \left(k_e^{n+1}\right)^{(m)}(i,\,j-1/2)\delta_y\left(T_e^{n+1}\right)^{(m)}(i,\,j-1/2)\right] \\ &+ \frac{1}{2\Delta y^2}\left[\left(k_e^{n}\right)^{(m)}(i,\,j+1/2)\delta_y\left(T_e^{n}\right)^{(m)}(i,\,j+1/2) - \left(k_e^{n}\right)^{(m)}(i,\,j-1/2)\delta_y\left(T_e^{n}\right)^{(m)}(i,\,j-1/2)\right] \\ &- G^{(m)}\left[\frac{(T_e^{n+1})^{(m)}(i,\,j)+(T_e^{n})^{(m)}(i,\,j)}{2} - \frac{(T_l^{n+1})^{(m)}(i,\,j)+(T_l^{n})^{(m)}(i,\,j)}{2}\right] \\ &+ Q^{n+\frac{1}{2}}(i,\,j)\end{aligned} \tag{31}$$

$$\begin{aligned}C_l^{(m)}\frac{1}{\Delta t}\Delta_{-t}\left(T_l^{n+1}\right)^{(m)}(i,\,j) &= G^{(m)}\left[\frac{(T_e^{n+1})^{(m)}(i,\,j)+(T_e^{n})^{(m)}(i,\,j)}{2} - \frac{(T_l^{n+1})^{(m)}(i,\,j)+(T_l^{n+1})^{(m)}(i,\,j)}{2}\right] \\ &- \left(3\lambda^{(m)}+2\mu^{(m)}\right)\alpha_T^{(m)}\left[\frac{\Delta_{-t}(\varepsilon_x^{n+1})^{(m)}(i,\,j)}{\Delta t} + \frac{\Delta_{-t}(\varepsilon_y^{n})^{(m)}(i,\,j)}{\Delta t}\right]\end{aligned} \tag{32}$$

$$\frac{1}{\Delta t}\Delta_{-t}\left(u^{n+1}\right)^{(m)}(i+1/2,\,j) = \left(v_1^{n+1}\right)^{(m)}(i+1/2,\,j) \tag{33}$$

$$\frac{1}{\Delta t}\Delta_{-t}\left(v^{n+1}\right)^{(m)}(i,\,j+1/2) = \left(v_2^{n+1}\right)^{(m)}(i,\,j+1/2) \tag{34}$$

where the boundary conditions are discretized as follows:

Table 1
Thermophysical properties [1,21,24]

Properties	Unit	Gold	Chromium
ρ	$\mathrm{kg\,m^{-3}}$	19 300	7190
E	Pa	77.97×10^{9}	279.45×10^{9}
Λ	$\mathrm{J\,m^{-3}\,K^{-2}}$	70	193.3
λ	Pa	199.0×10^{9}	83.3×10^{9}
μ	Pa	27.0×10^{9}	115.0×10^{9}
α_T	$\mathrm{K^{-1}}$	14.2×10^{-6}	4.9×10^{-6}
C_{e0}	$\mathrm{J\,m^{-3}\,K^{-1}}$	2.1×10^{4}	5.8×10^{4}
C_l	$\mathrm{J\,m^{-3}\,K^{-1}}$	2.5×10^{6}	3.3×10^{6}
G	$\mathrm{W\,m^{-3}\,K^{-1}}$	2.6×10^{16}	42×10^{16}
K_e	$\mathrm{W\,m^{-1}\,K^{-1}}$	315	94

$$\left(\sigma_x^{n+1}\right)^{(1)}(1,j)=0,\quad \left(\sigma_x^{n+1}\right)^{(2)}(N+1,j)=0$$
$$\left(\sigma_{xy}^{n+1}\right)^{(1)}(1,j)=0,\quad \left(\sigma_{xy}^{n+1}\right)^{(2)}(N+1,j)=0$$
$$1\leqslant j\leqslant M+1 \tag{35}$$

$$\left(\sigma_y^{n+1}\right)^{(1)}(i,1)=0,\quad \left(\sigma_y^{n+1}\right)^{(2)}(i,M+1)=0$$
$$\left(\sigma_{xy}^{n+1}\right)^{(1)}(i,1)=0,\quad \left(\sigma_{xy}^{n+1}\right)^{(2)}(i,M+1)=0$$
$$1\leqslant i\leqslant N+1 \tag{36}$$

$$\left(T_e^{n+1}\right)^{(1)}(1,j)=\left(T_e^{n+1}\right)^{(1)}(2,j)$$
$$\left(T_e^{n+1}\right)^{(2)}(N+1,j)=\left(T_e^{n+1}\right)^{(2)}(N,j)$$
$$1\leqslant j\leqslant M+1 \tag{37a}$$

$$\left(T_e^{n+1}\right)^{(m)}(i,1)=\left(T_e^{n+1}\right)^{(m)}(i,2)$$
$$\left(T_e^{n+1}\right)^{(m)}(i,M+1)=\left(T_e^{n+1}\right)^{(m)}(i,M)$$
$$1\leqslant i\leqslant N+1 \tag{37b}$$

$$\left(T_l^{n+1}\right)^{(1)}(1,j)=\left(T_l^{n+1}\right)^{(1)}(2,j),$$
$$\left(T_l^{n+1}\right)^{(2)}(N+1,j)=\left(T_l^{n+1}\right)^{(2)}(N,j)$$
$$1\leqslant j\leqslant M+1 \tag{38a}$$

$$\left(T_l^{n+1}\right)^{(m)}(i,1)=\left(T_l^{n+1}\right)^{(m)}(i,2),$$
$$\left(T_l^{n+1}\right)^{(m)}(i,M+1)=\left(T_l^{n+1}\right)^{(m)}(i,M)$$
$$1\leqslant i\leqslant N+1 \tag{38b}$$

for any time level n and $m=1,2$.

From Eqs. (10) and (12), we discretize interfacial conditions for electron temperature and velocity as follows:

$$k_e^{(1)}\frac{(T_e^{n+1})^{(1)}(N+1,j)-(T_e^{n+1})^{(1)}(N,j)}{\Delta x}=k_e^{(2)}\frac{(T_e^{n+1})^{(2)}(2,j)-(T_e^{n+1})^{(2)}(1,j)}{\Delta x} \tag{39a}$$

$$-k_e^{(1)}\frac{(T_e^{n+1})^{(1)}(N+1,j)-(T_e^{n+1})^{(1)}(N,j)}{\Delta x}=\sigma\left\{\left[\left(T_e^{n+1}\right)^{(1)}(N+1,j)\right]^4-\left[\left(T_e^{n+1}\right)^{(2)}(1,j)\right]^4\right\} \tag{39b}$$

$$\mu^{(1)}\left(v_1^{n+1}\right)^{(1)}(N+1,j)=\mu^{(2)}\left(v_1^{n+1}\right)^{(2)}(1,j) \tag{40a}$$

$$\mu^{(1)}\left(v_2^{n+1}\right)^{(1)}(N+1,j)=\mu^{(2)}\left(v_2^{n+1}\right)^{(2)}(1,j) \tag{40b}$$

From Eq. (19), we obtain discrete schemes for strains at interface:

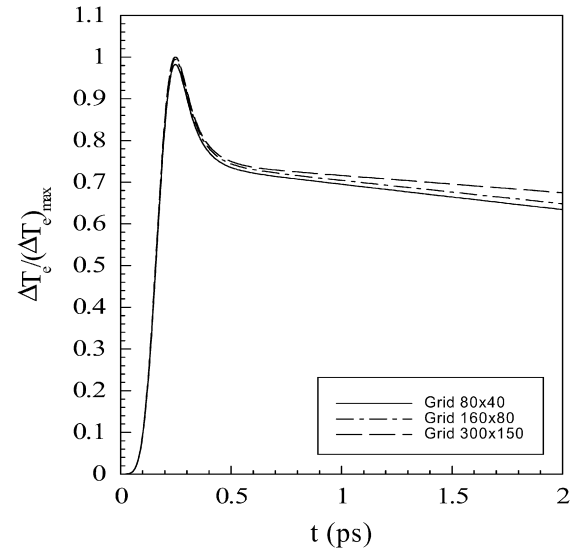

(a)

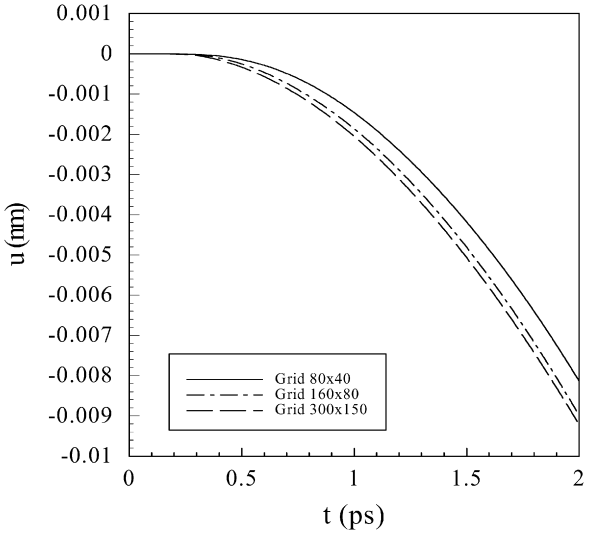

(b)

Fig. 3. Change in electron temperature at $x=0$ and $y=0$ and displacement (u) at $x=\frac{1}{2}\Delta x$ and $y=\Delta y$ versus time for various meshes (80×40, 160×80, and 300×150).

$$\left(\varepsilon_x^{n+1}\right)^{(1)}(N+1,j)=\frac{(v_1^{n+1})^{(1)}(N+1,j)-(v_1^{n+1})^{(1)}(N,j)}{\Delta x/2}\Delta t+\left(\varepsilon_x^{n}\right)^{(1)}(N+1,j) \tag{41a}$$

$$\left(\varepsilon_x^{n+1}\right)^{(2)}(1,j)=\frac{(v_1)^{(2)}(2,j)-(v_1)^{(2)}(1,j)}{\Delta x/2}\Delta t+\left(\varepsilon_x^{n}\right)^{(2)}(1,j) \tag{41b}$$

$$\left(\varepsilon_y^{n+1}\right)^{(1)}(N+1,j)=\frac{(v_2)^{(1)}(N+1,j)-(v_2)^{(1)}(N+1,j-1)}{\Delta y}\Delta t+\left(\varepsilon_y^{n}\right)^{(1)}(N+1,j) \tag{42a}$$

$$\left(\varepsilon_y^{n+1}\right)^{(2)}(1,j)=\frac{(v_2)^{(2)}(2,j)-(v_2)^{(2)}(1,j-1)}{\Delta y}\Delta t+\left(\varepsilon_y^{n}\right)^{(2)}(1,j) \tag{42b}$$

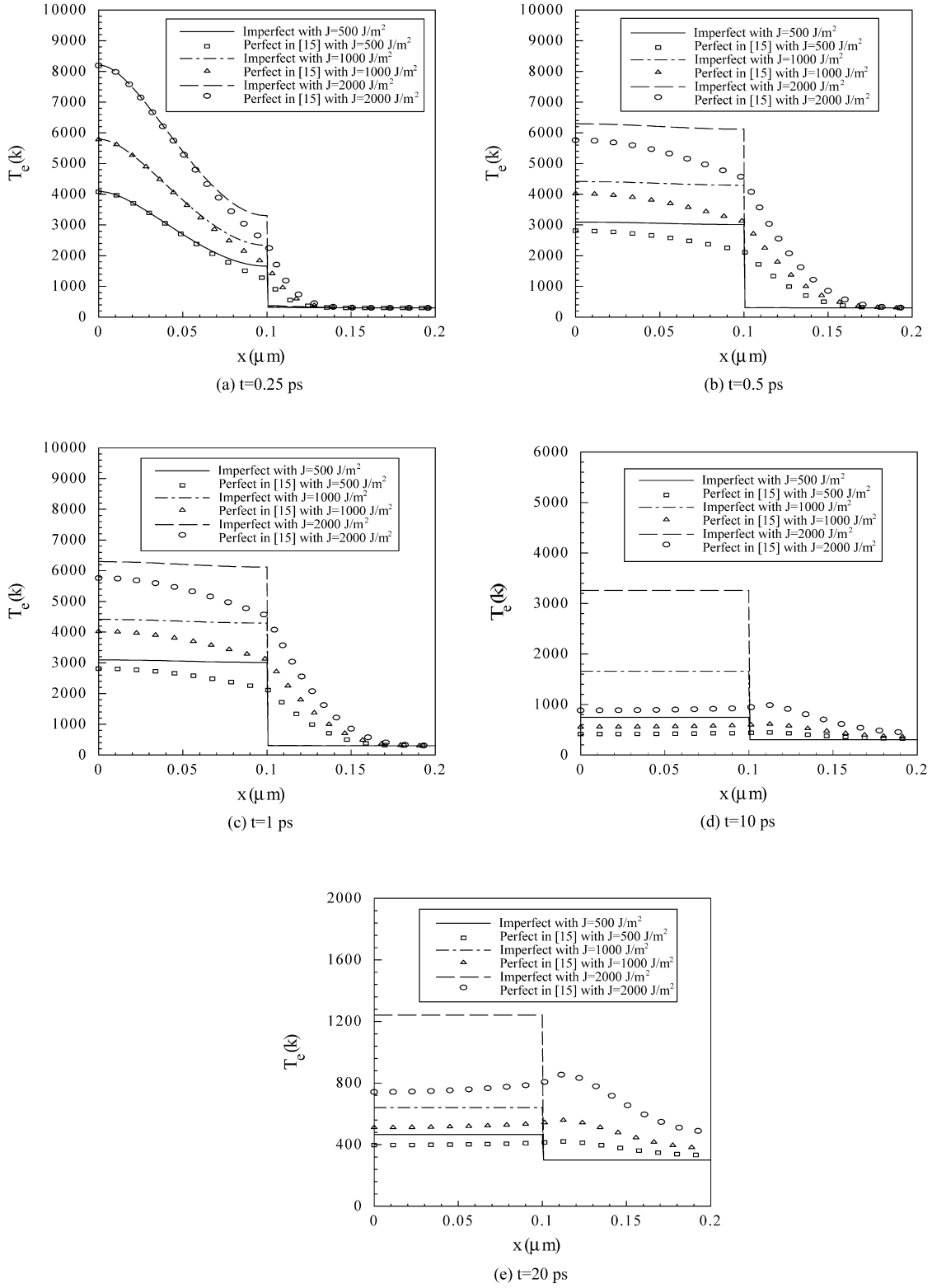

Fig. 4. Comparison of electron temperature at $y = 0$ at different times between perfect [15] and imperfect contact at interface with three different laser fluences.

$$\left(\gamma_{xy}^{n+1}\right)^{(1)}(N+1,j) = \frac{\Delta t}{\Delta y}\left[\left(v_1^{n+1}\right)^{(1)}(N+1,j+1) - \left(v_1^{n+1}\right)^{(1)}(N+1,j)\right] + \frac{\Delta t}{\Delta x}\left[\left(v_2^{n+1}\right)^{(1)}(N+1,j) - \left(v_2^{n+1}\right)^{(1)}(N,j)\right] + \left(\gamma_{xy}^{n}\right)^{(1)}(N+1,j) \tag{43a}$$

$$\left(\gamma_{xy}^{n+1}\right)^{(2)}(1,j) = \frac{\Delta t}{\Delta y}\left[\left(v_1^{n+1}\right)^{(2)}(1,j+1) - \left(v_1^{n+1}\right)^{(2)}(1,j)\right]$$

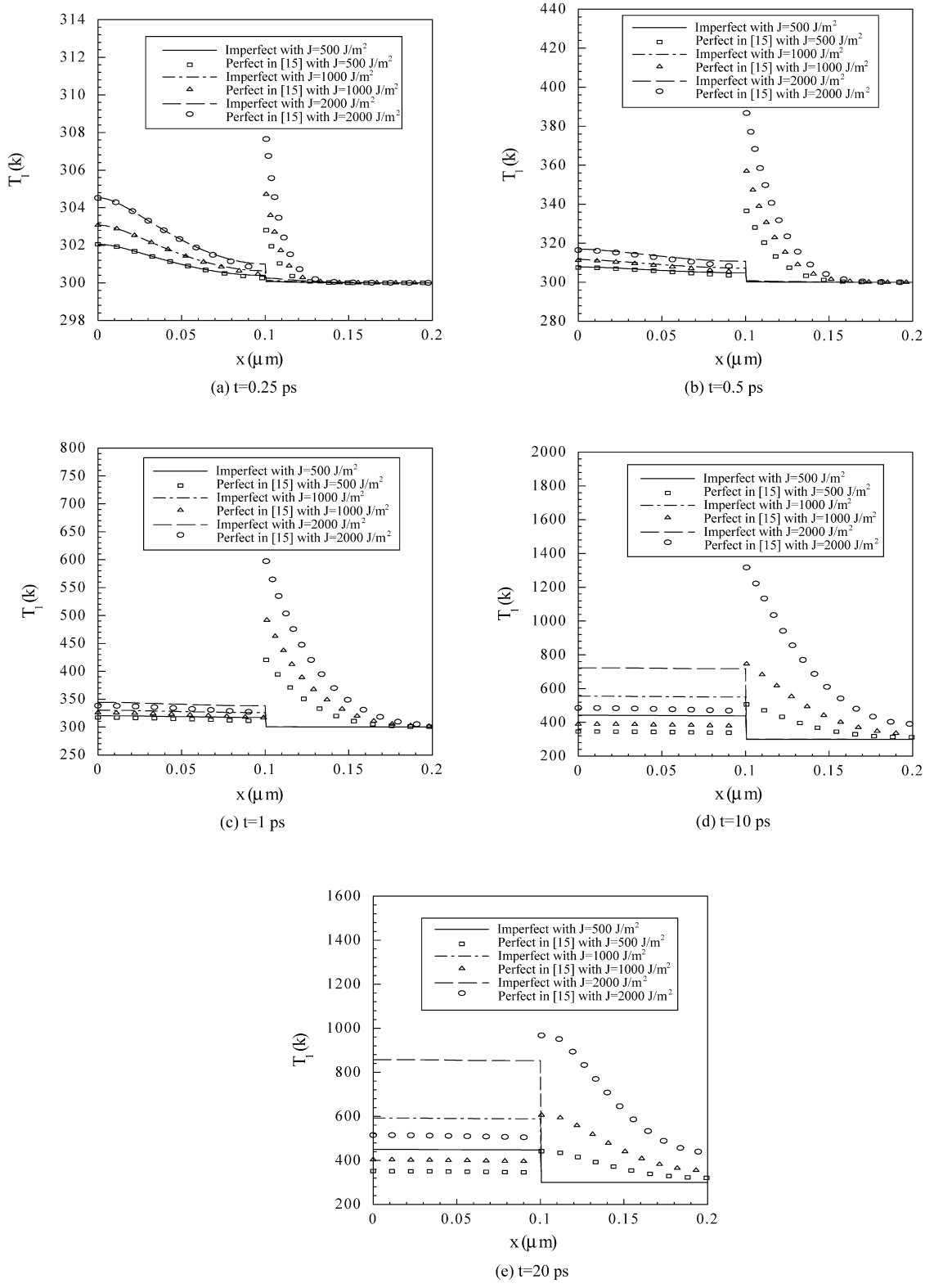

Fig. 5. Comparison of lattice temperature at $y = 0$ at different times between perfect [15] and imperfect contact at interface with three different laser fluences.

$$+\frac{\Delta t}{\Delta x}\left[\left(v_2^{n+1}\right)^{(2)}(2,j)-\left(v_2^{n+1}\right)^{(2)}(1,j)\right]+\left(\gamma_{xy}^{n}\right)^{(2)}(1,j) \tag{43b}$$

From Eqs. (4) and (13), we obtain a discrete interfacial condition for lattice temperature:

$$\frac{\mu^{(1)}}{E^{(1)}}\left\{\left(\lambda^{(1)}+2\mu^{(1)}\right)\left(\varepsilon_x^{n+1}\right)^{(1)}(N+1,j)+\lambda^{(1)}\left(\varepsilon_y^{n+1}\right)^{(1)}(N+1,j)-\left(3\lambda^{(1)}+2\mu^{(1)}\right)\alpha_T^{(1)}\left[\left(T_l^{n+1}\right)^{(1)}(N+1,j)-T_0\right]\right\}$$

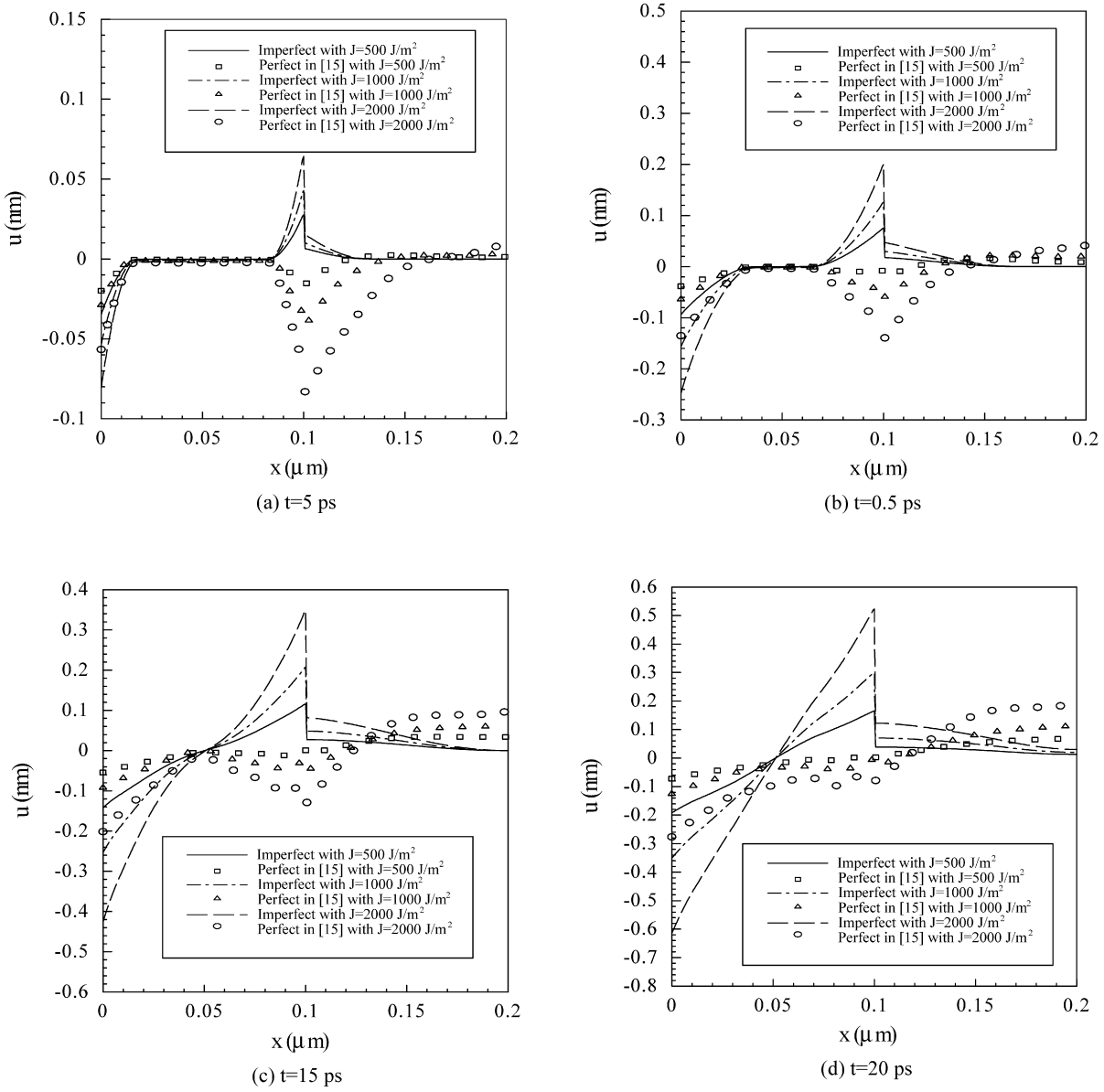

Fig. 6. Comparison of displacement (u) at $y = \Delta y$ at different times between perfect [15] and imperfect contact at interface with three different laser fluences.

$$= \frac{\mu^{(2)}}{E^{(2)}}\left\{\left(\lambda^{(2)}+2\mu^{(2)}\right)\left(\varepsilon_x^{n+1}\right)^{(2)}(1,j)+\lambda^{(2)}\left(\varepsilon_y^{n+1}\right)^{(2)}(1,j) - \left(3\lambda^{(2)}+2\mu^{(2)}\right)\alpha_T^{(2)}\left[\left(T_l^{n+1}\right)^{(2)}(1,j)-T_0\right]\right\} \quad (44)$$

Furthermore, from Eqs. (6) and (11) we have

$$\mu^{(1)}\left(\gamma_{xy}^{n+1}\right)^{(1)}(N+1,j) = \mu^{(2)}\left(\gamma_{xy}^{n+1}\right)^{(2)}(1,j) \quad (45)$$

where $1 \leqslant j \leqslant M+1$.

The initial conditions are assumed to be

$$\left(u^0\right)^{(m)}(i+1/2,j)=0, \quad \left(v^0\right)^{(m)}(i,j+1/2)=0 \quad (46a)$$

$$\left(v_1^0\right)^{(m)}(i+1/2,j)=0, \quad \left(v_1^0\right)^{(m)}(i,j+1/2)=0 \quad (46b)$$

$$\left(T_e^0\right)^{(m)}(i,j)=0, \quad \left(T_l^0\right)^{(m)}(i,j)=0 \quad (46c)$$

$$1 \leqslant i \leqslant N+1,\ 1 \leqslant j \leqslant M+1,\ m=1,2$$

The interfacial values are calculated in this order. From Eq. (39b), $(T_e^{n+1})^{(1)}(N+1,j)$ is solved iteratively:

$$\left[\left(T_e^{n+1}\right)^{(1)}(N+1,j)\right]^{\text{new}} = -\frac{\sigma\Delta x}{k_e^{(1)}}\left\{\left\{\left[\left(T_e^{n+1}\right)^{(1)}(N+1,j)\right]^{\text{old}}\right\}^4 - \left\{\left[\left(T_e^{n+1}\right)^{(2)}(1,j)\right]^{\text{old}}\right\}^4\right\} + \left[\left(T_e^{n+1}\right)^{(1)}(N,j)\right]^{\text{old}} \quad (47)$$

and then $(T_e^{n+1})^{(2)}(1,j)$ is solved based on Eq. (39a):

$$\left[\left(T_e^{n+1}\right)^{(2)}(1,j)\right]^{\text{new}} = \left[\left(T_e^{n+1}\right)^{(2)}(2,j)\right]^{\text{old}} - \frac{k_e^{(1)}}{k_e^{(2)}}\left\{\left[\left(T_e^{n+1}\right)^{(1)}(N+1,j)\right]^{\text{old}} - \left[\left(T_e^{n+1}\right)^{(1)}(N,j)\right]^{\text{old}}\right\} \quad (48)$$

Once updated $(T_e^{n+1})^{(1)}(N+1,j)$ and $(T_e^{n+1})^{(2)}(1,j)$ are obtained, we substitute them into Eq. (32) to obtain updated $(T_l^{n+1})^{(1)}(N+1,j)$ and $(T_l^{n+1})^{(2)}(1,j)$. We then substitute Eqs. (40a), (40b), (41a), (41b), (42a) and (42b) into Eq. (44)

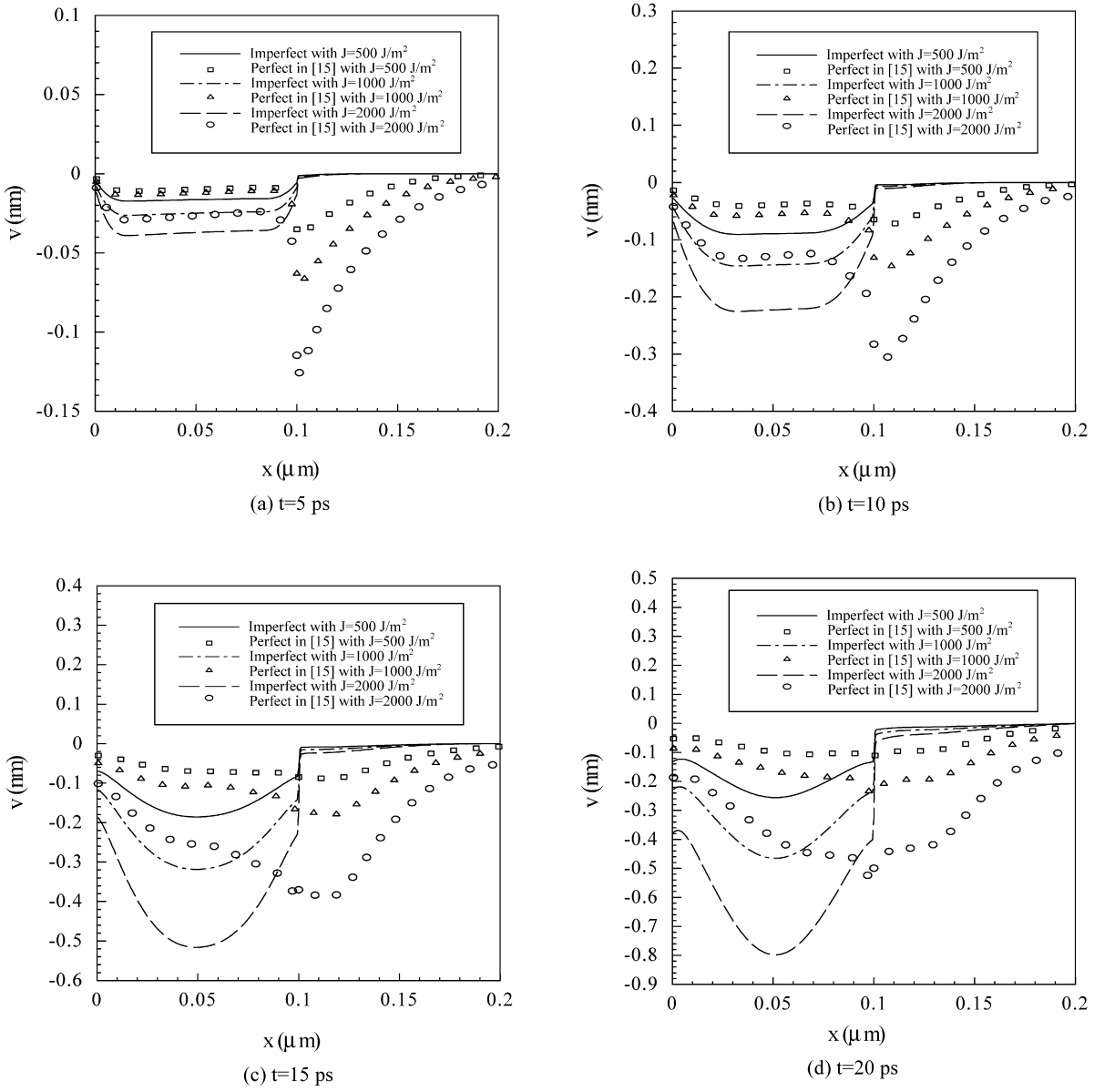

Fig. 7. Comparison of displacement (v) at $y = \frac{1}{2}\Delta y$ at different times between perfect [15] and imperfect contact at interface with three different laser fluences.

to obtain updated $(v_1^{n+1})^{(1)}(N+1, j)$ and $(v_1^{n+1})^{(2)}(1, j)$, and substitute Eqs. (40a), (40b), (43a) and (43b) into Eq. (45) to obtain updated $(v_2^{n+1})^{(1)}(N+1, j)$ and $(v_2^{n+1})^{(2)}(1, j)$. Finally, from the above known interfacial values, we obtain updated $(u^{n+1})^{(m)}$, $(v^{n+1})^{(m)}$, $(\varepsilon_x^{n+1})^{(m)}$, $(\varepsilon_y^{n+1})^{(m)}$, $(\gamma_{xy}^{n+1})^{(m)}$, $(\sigma_x^{n+1})^{(m)}$, $(\sigma_y^{n+1})^{(m)}$, $(\sigma_{xy}^{n+1})^{(m)}$ at interface.

It can be seen that the truncation error of Eqs. (23) and (24) is $O(\Delta t + \Delta x^2 + \Delta y^2)$ and the truncation error of Eqs. (31) and (32) is $O(\Delta t^2 + \Delta x^2 + \Delta y^2)$. It should be pointed out that Eqs. (23) and (24) are nonlinear since the terms $\delta_x[(T_e^2)^{n+1}]^{(m)}(i+1/2, j)$ and $\delta_y[(T_e^2)^{n+1}]^{(m)}(i, j+1/2)$ are nonlinear. Also, it can be seen that Eqs. (31) and (39b) are nonlinear. Therefore, the above scheme must be solved iteratively. An iterative method for solving the above scheme at time level $n+1$ can be described as follows:

Step 1. Guess $(\varepsilon_x^{n+1})^{(m)}$, $(\varepsilon_y^{n+1})^{(m)}$ and $(\gamma_{xy}^{n+1})^{(m)}$, solve Eqs. (31), (32), (47), and (48) iteratively for $(T_e^{n+1})^{(m)}$ and $(T_l^{n+1})^{(m)}$.

Step 2. Solve for $(\sigma_x^{n+1})^{(m)}$, $(\sigma_y^{n+1})^{(m)}$, $(\sigma_{xy}^{n+1})^{(m)}$ using Eqs. (28)–(30).

Step 3. Solve for $(v_1^{n+1})^{(m)}$ and $(v_2^{n+1})^{(m)}$ using Eqs. (23) and (24).

Step 4. Update $(\varepsilon_x^{n+1})^{(m)}$, $(\varepsilon_y^{n+1})^{(m)}$ and $(\gamma_{xy}^{n+1})^{(m)}$ using Eqs. (25)–(27).

Step 5. Repeat the above steps until a convergent solution is obtained based on the following criteria:

$$\max_{i,j}\left|\left[\left(T_e^{n+1}\right)^{(1)}(i,j)\right]^{\text{new}} - \left[\left(T_e^{n+1}\right)^{(1)}(i,j)\right]^{\text{old}}\right| < \epsilon_1$$

$$\max_{i,j}\left|\left[\left(\varepsilon_x^{n+1}\right)^{(m)}(i,j)\right]^{\text{new}} - \left[\left(\varepsilon_x^{n+1}\right)^{(m)}(i,j)\right]^{\text{old}}\right| < \epsilon_2$$

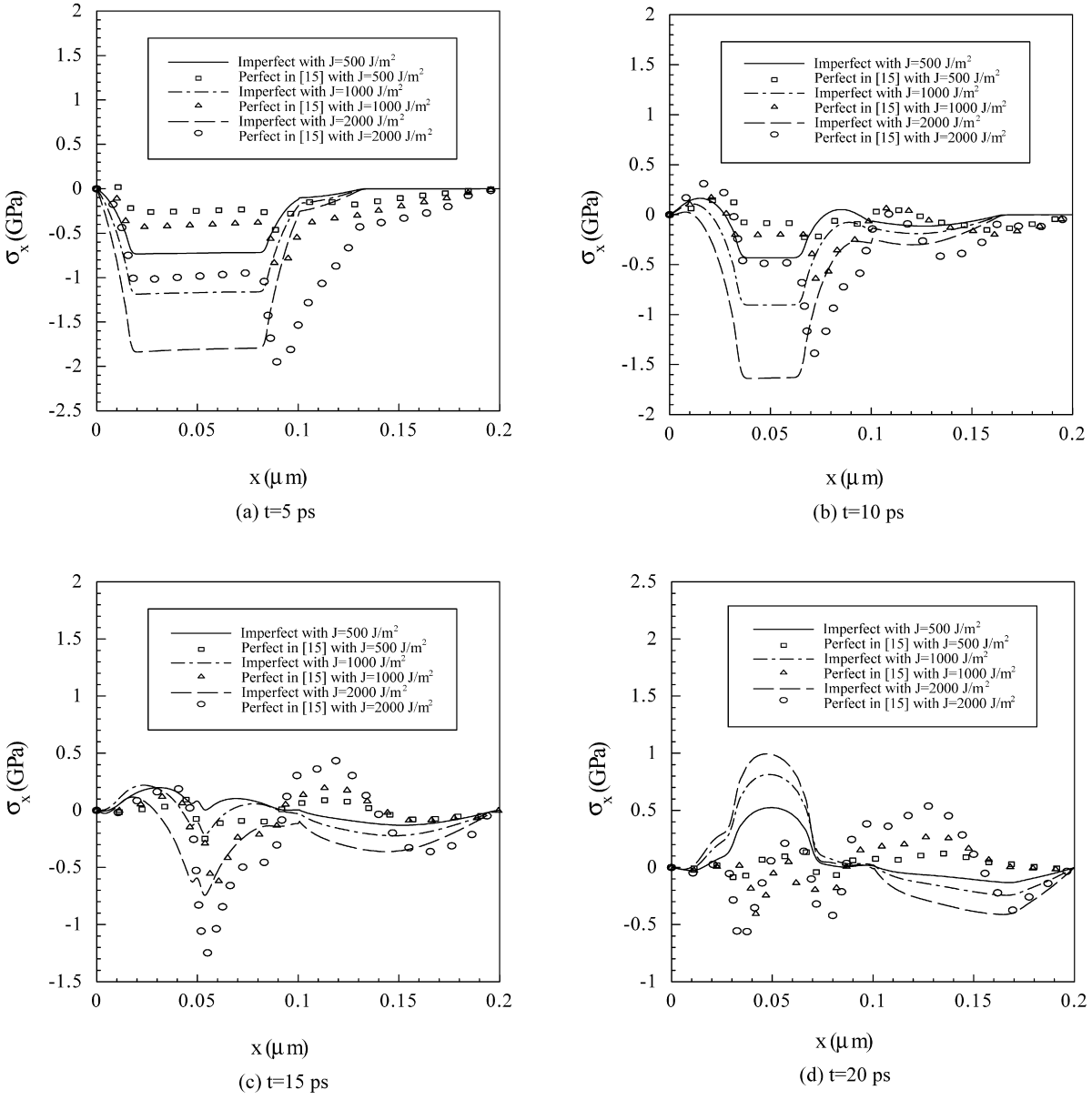

Fig. 8. Comparison of normal stress (σ_x) at $y = \Delta y$ at different times between perfect [15] and imperfect contact at interface with three different laser fluences.

$$\max_{i,j}\left|\left[\left(\varepsilon_y^{n+1}\right)^{(m)}(i,j)\right]^{\text{new}} - \left[\left(\varepsilon_y^{n+1}\right)^{(m)}(i,j)\right]^{\text{old}}\right| < \epsilon_2$$

$$\max_{i,j}\left|\left[\left(\gamma_{xy}^{n+1}\right)^{(m)}(i,j)\right]^{\text{new}} - \left[\left(\gamma_{xy}^{n+1}\right)^{(m)}(i,j)\right]^{\text{old}}\right| < \epsilon_2$$

4. Numerical example

To test the applicability of the developed numerical scheme, we investigated the temperature rise and thermal deformation in a double-layered thin film consisting of a gold layer padding on a chromium layer with the dimensions 0.1 μm (thickness) × 1 μm (length) each layer, as shown in Fig. 1. The thermophysical properties for gold and chromium are listed in Table 1 [1,21,24]. Three meshes of 80 × 40, 160 × 80, 300 × 150 were chosen in order to test the convergence of the scheme. The time increment was chosen to be 0.005 ps and T_0 was set to be 300 K. The values of those parameters for laser were chosen to be $R = 0.93$, $t_p = 0.1 \times 10^{-12}$ s, $x_s = 15.3 \times 10^{-9}$ m, and $y_s = 1.0 \times 10^{-6}$ m [1,21]. Three different values of laser fluences ($J = 500\ \text{J m}^{-2}$, $1000\ \text{J m}^{-2}$ and $2000\ \text{J m}^{-2}$) were chosen to study the hot-electron blast force. The convergence criteria were chosen to be $\epsilon_1 = 10^{-8}$ for temperature and $\epsilon_2 = 10^{-16}$ for thermal deformation, respectively. Figs. 4–15 were plotted from the data obtained based on the mesh of 160 × 80.

Fig. 3(a) shows the temperature change in electron temperature $(\Delta T_e/(\Delta T_e)_{\max})$ at $x = 0$ and $y = 0$ with laser fluence $J = 1000\ \text{J m}^{-2}$. The maximum temperature rise of $T_e^{(1)}$ (i.e., $(\Delta T_e)_{\max}$) is about 5823 K. Fig. 3(b) shows the displacement (u) at $x = \frac{1}{2}\Delta x$ and $y = \Delta y$ versus time. It can be seen from both figures that mesh size had no significant effect on the so-

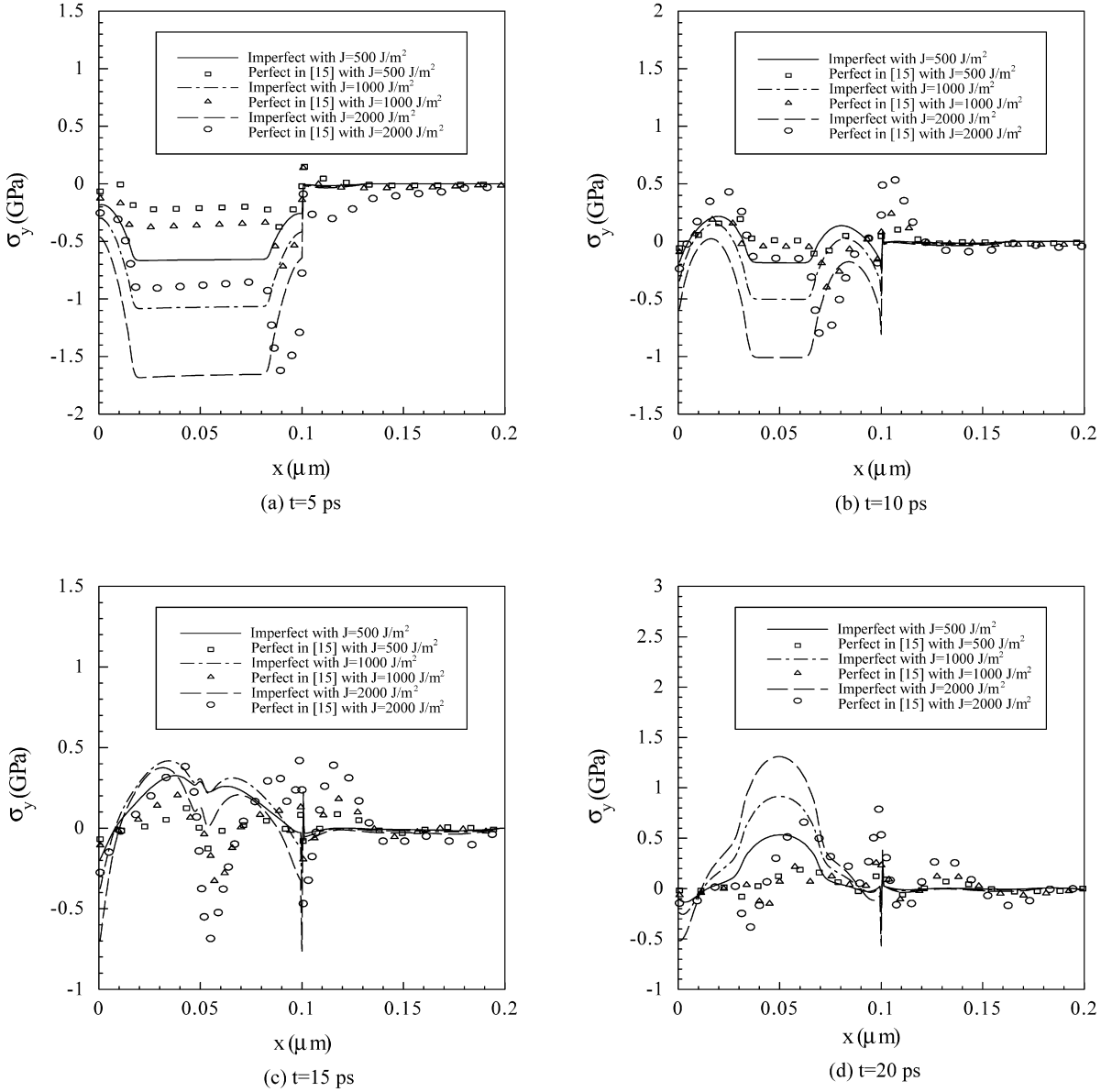

Fig. 9. Comparison of normal stress (σ_y) at $y = \Delta y$ at different times between perfect [15] and imperfect contact at interface with three different laser fluences.

lution and hence this method is only weakly dependent on the grid.

Figs. 4 and 5 show comparisons of electron temperature and lattice temperature along x at $y = 0$ between the perfect thermal contact [15] and the imperfect thermal contact at interface with three different laser fluences ($J = 500\ \mathrm{J\,m^{-2}}$, $1000\ \mathrm{J\,m^{-2}}$, $2000\ \mathrm{J\,m^{-2}}$) at different times (a) $t = 0.25$ ps, (b) $t = 0.5$ ps, (c) $t = 1$ ps, (d) $t = 10$ ps, and (e) $t = 20$ ps, respectively. It can be seen that the electron temperature rises to its maximum at the beginning and then decreases while the lattice temperature rises gradually with time. Fig. 4 shows clearly that there is a sharp discontinuity of electron temperature at the interface when imperfect thermal contact exists between two bonded thin layers. Similar temperature discontinuity is observed at the interface for lattice temperature in Fig. 5. These results indicate that imperfect thermal contact at the interface provides a barrier to thermal energy diffusion across the interface. These two figures also show that electron temperature and lattice temperature are uniform throughout the chromium layer, and uniform throughout the gold layer after a long period. The uniform electron and lattice temperatures are probably due to increased rate of collision between electrons and phonons in the gold layer as electron energy diffusion is inhibited at the interface.

Figs. 6 and 7 show comparisons of displacement u (thickness direction) at $y = \Delta y$ and v (length direction) along x at $y = \frac{1}{2}\Delta y$ between the perfect thermal contact [15] and the imperfect thermal contact at interface with three different laser fluences ($J = 500\ \mathrm{J\,m^{-2}}$, $1000\ \mathrm{J\,m^{-2}}$, $2000\ \mathrm{J\,m^{-2}}$) at different times (a) $t = 5$ ps, (b) $t = 10$ ps, (c) $t = 15$ ps, and (d) $t = 20$ ps, respectively. It can be seen that for the imperfect thermal contact case sharp discontinuity of displacement ex-

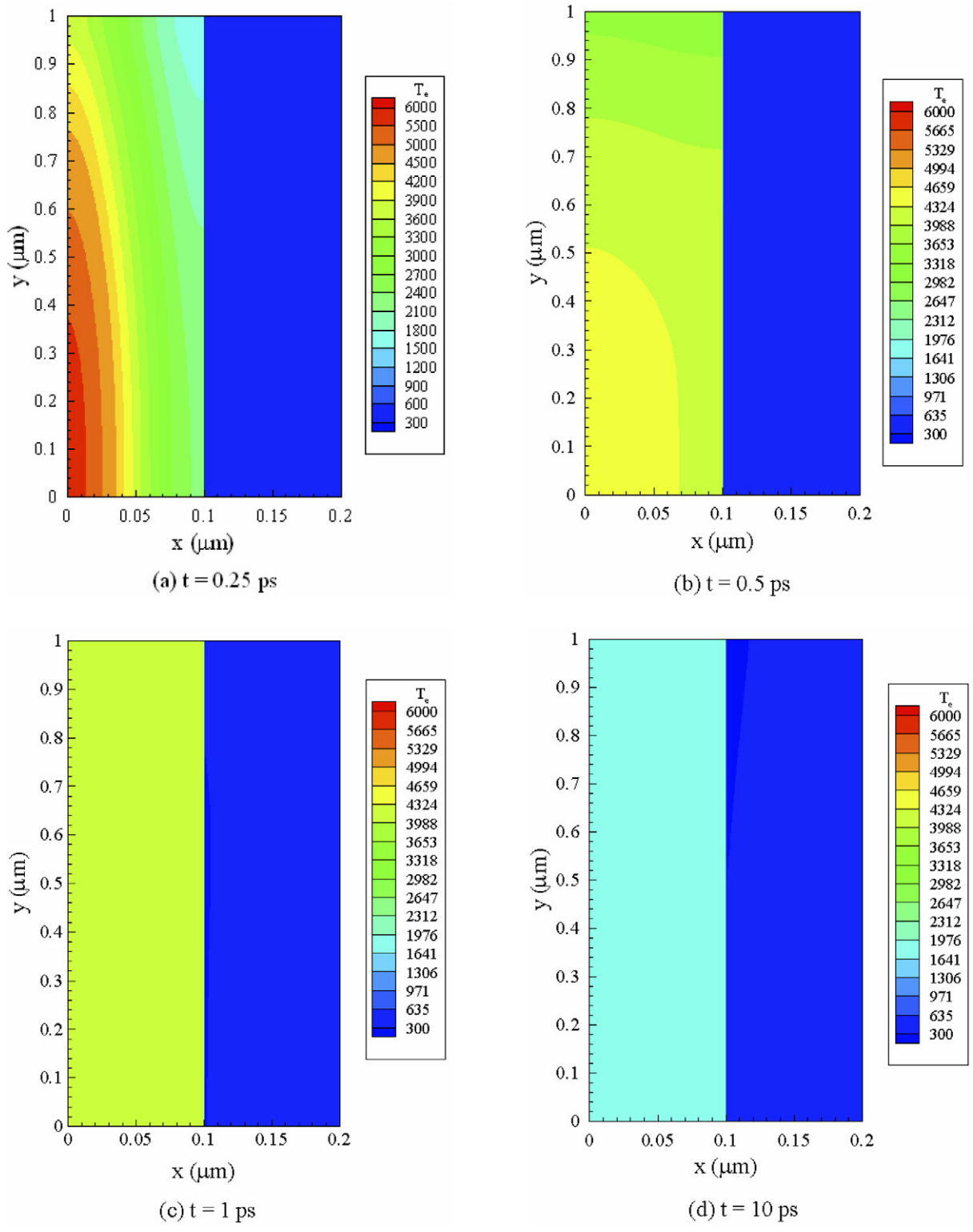

Fig. 10. Electron temperature (K) profiles at different times with laser fluence $J = 1000\ \mathrm{J\,m^{-2}}$.

ists at the interface, and the gold layer undergoes severe displacement alteration from negative to positive while the displace alteration in the chromium layer is almost absent. However, sharp discontinuity of displacement exists at the interface may result in shear failure. Severe displacement alteration exists in the gold layer may produce internal damages within the layer. Displacement alteration in the gold layer is more pronounced for bonded films with the imperfect thermal contact.

Figs. 8 and 9 show comparisons of normal stress σ_x (thickness direction) at $y = \Delta y$ and σ_y (length direction) along x at $y = \Delta y$ between the perfect thermal contact [15] and the im-

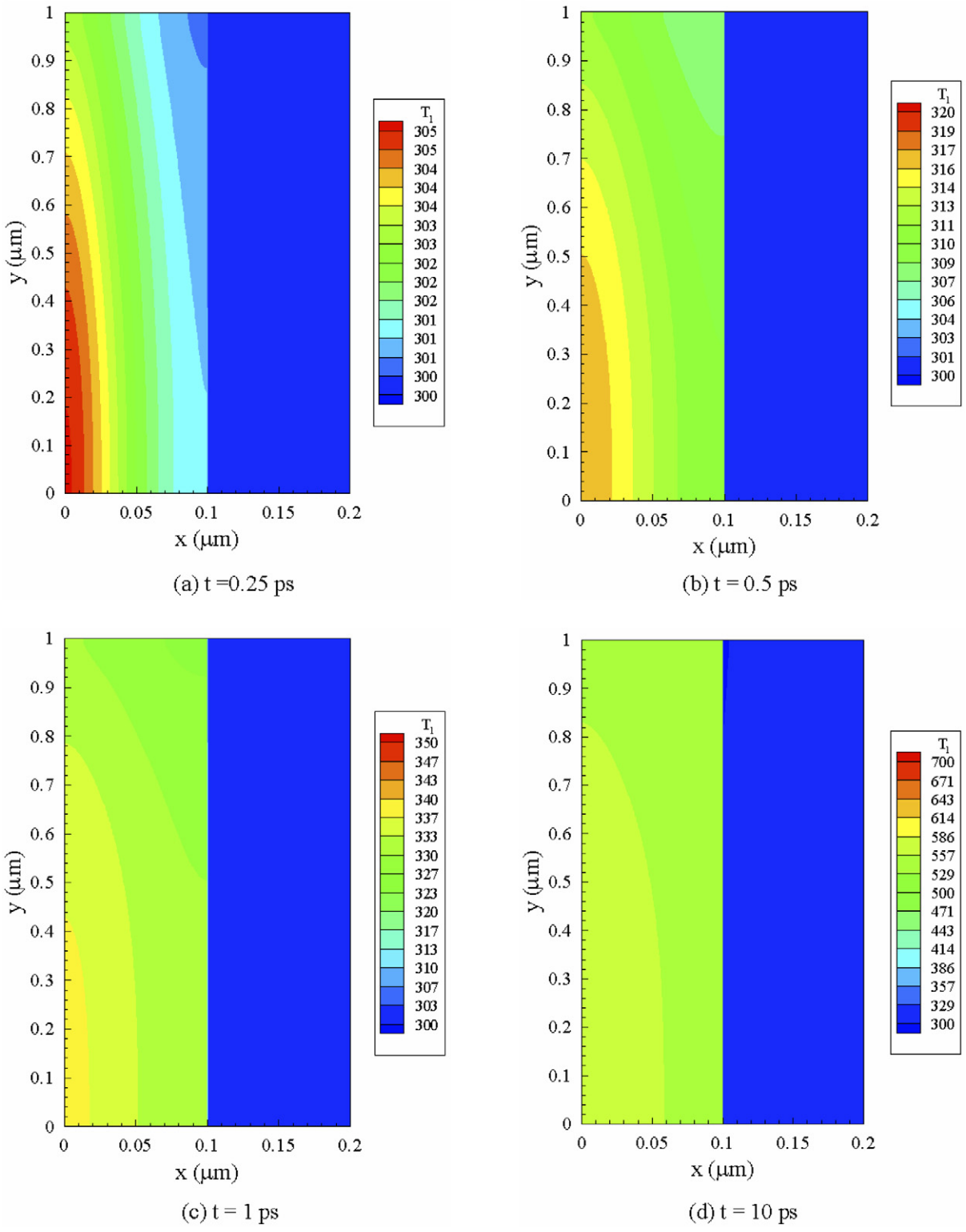

Fig. 11. Lattice temperature (K) profiles at different times with laser fluence $J = 1000\ \mathrm{J\,m^{-2}}$.

perfect thermal contact at interface with three different laser fluences ($J = 500\ \mathrm{J\,m^{-2}}$, $1000\ \mathrm{J\,m^{-2}}$, $2000\ \mathrm{J\,m^{-2}}$) at different times (a) $t = 5$ ps, (b) $t = 10$ ps, (c) $t = 15$ ps, and (d) $t = 20$ ps, respectively. The ultrashort-pulsed laser heating produced severe stress distributions in the gold layer for the imperfect thermal contact case. However, in the chromium layer, stress distribution is less severe. This implies that the gold layer may undergo severe structural deformation. Furthermore, it can be seen from Fig. 8 that the normal stress σ_x does not show non-physical oscillations, as shown in Fig. 5 [16].

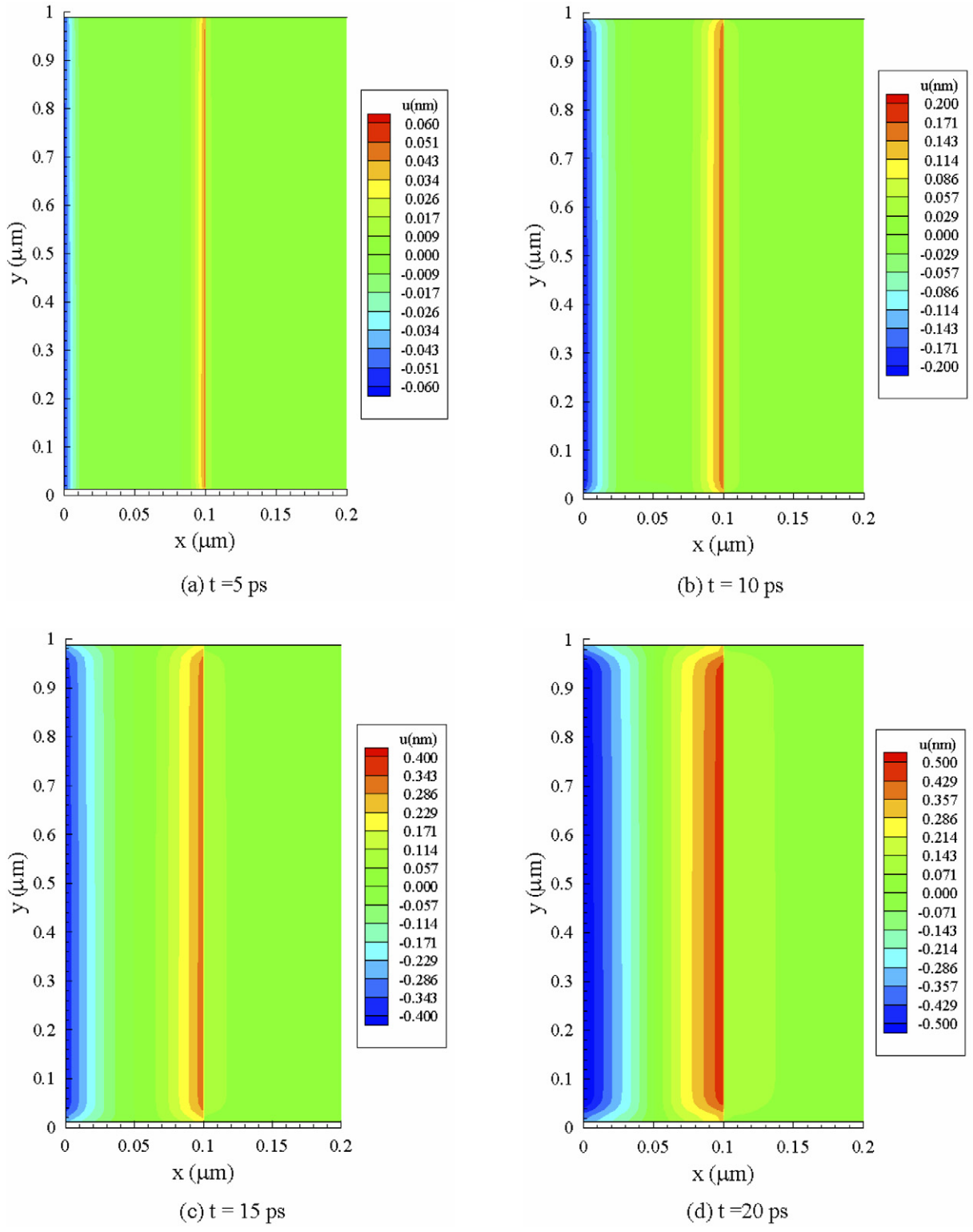

Fig. 12. Displacement (u) profiles at different times with laser fluence $J = 1000\ \mathrm{J\,m^{-2}}$.

Figs. 10 and 11 show contours of electron temperature profile and lattice temperature profile with the laser fluence of $J = 1000\ \mathrm{J\,m^{-2}}$ at different times (a) $t = 0.25$ ps, (b) $t = 0.5$ ps, (c) $t = 1$ ps and (d) $t = 10$ ps, respectively. Figs. 12–15 show contours of displacement u (thickness direction) profile, displacement v (length direction) profile, normal stress σ_x (thickness direction) profile, and normal stress σ_y (length direction) profile with the laser fluence of $J = 1000\ \mathrm{J\,m^{-2}}$ at different times (a) $t = 5$ ps, (b) $t = 10$ ps, (c) $t = 15$ ps, and (d) $t = 20$ ps, respectively.

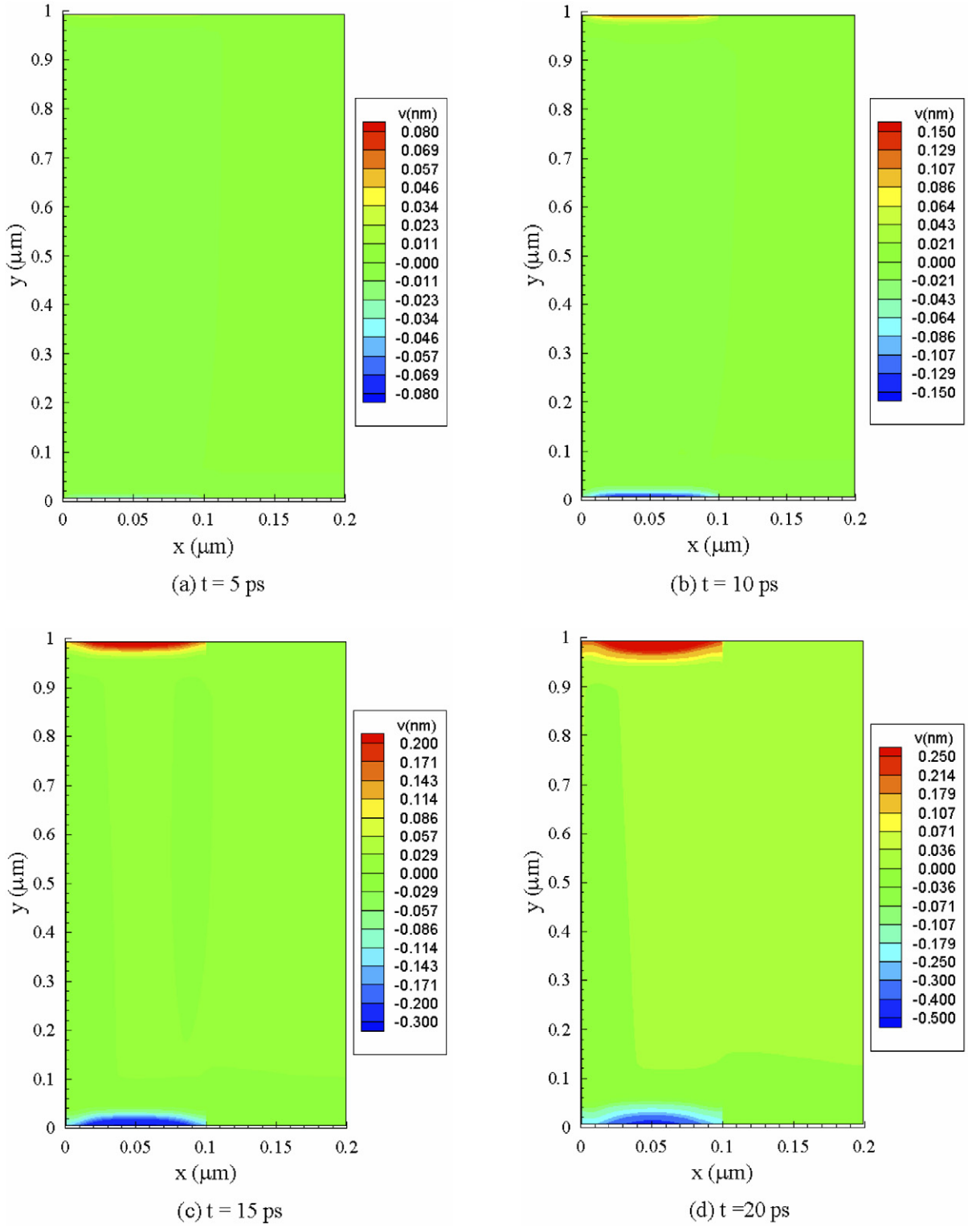

Fig. 13. Displacement (v) profiles at different times with laser fluence $J = 1000\ \mathrm{J\,m^{-2}}$.

5. Conclusion

We have developed a finite difference method for studying thermal deformation in a double-layered thin film with imperfect thermal contact at interface, which is exposed to ultrashort pulsed lasers. The method, based on the parabolic two-step heat transport equations, accounts for the coupling effect between lattice temperature and strain rate, as well as for the hot-electron blast effect in momentum transfer. By introducing the velocity components into the dynamic equations of motion and using a staggered grid, the method allows us to avoid non-physical oscillations in the solution.

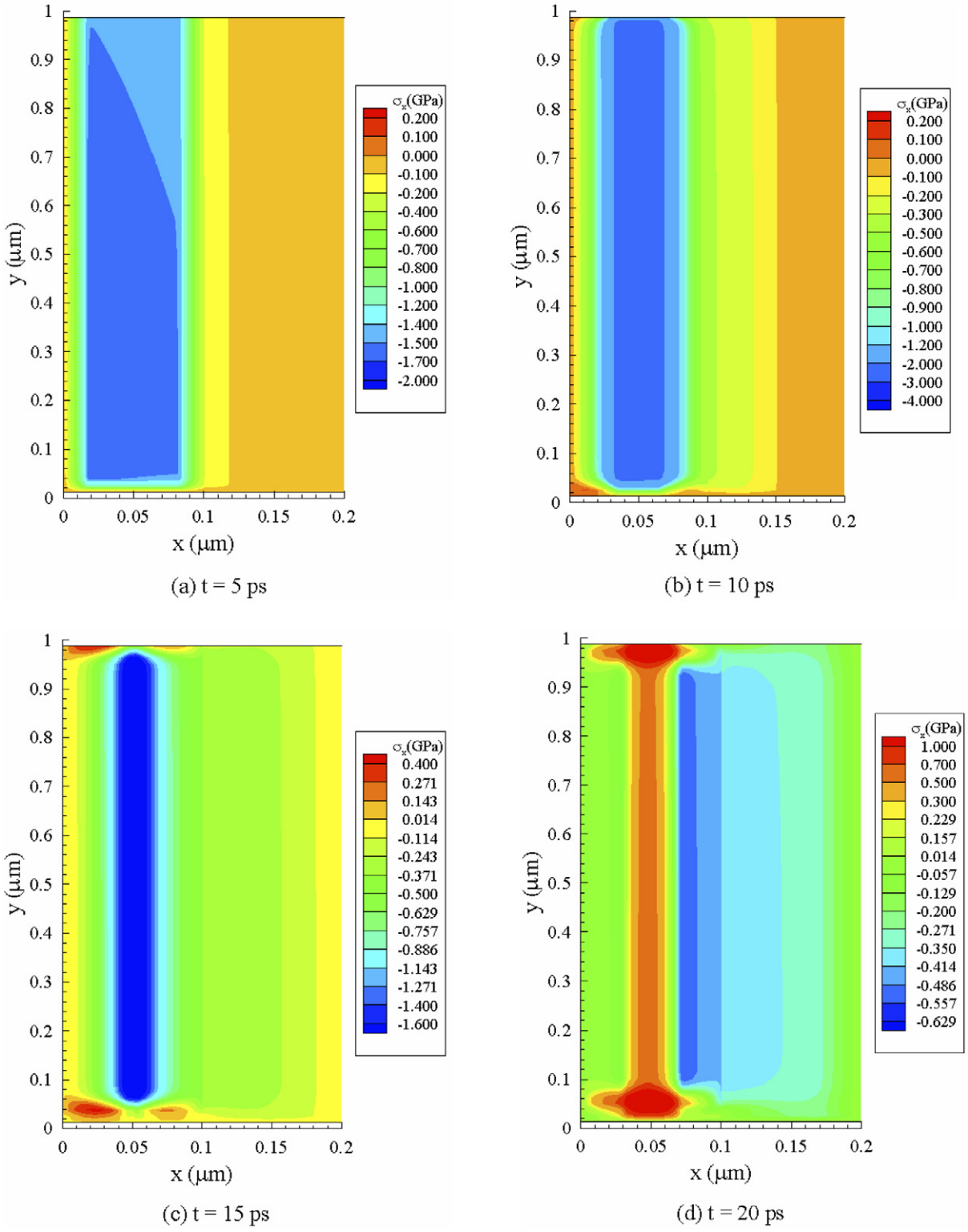

Fig. 14. Normal stress (σ_x) profiles at different times with laser fluence $J = 1000\ \mathrm{J\,m^{-2}}$.

Numerical results show that there is a sharp discontinuity of electron temperature at the interface when imperfect thermal contact exists between two bonded thin layers, and similar temperature discontinuity is observed at the interface for lattice temperature. These results indicate that imperfect thermal contact at the interface provides a barrier to thermal energy diffusion across the interface. The observed uniform electron and lattice temperatures are probably due to increased rate of collision between electrons and phonons in the gold layer as electron energy diffusion is inhibited at the interface. Sharp discontinu-

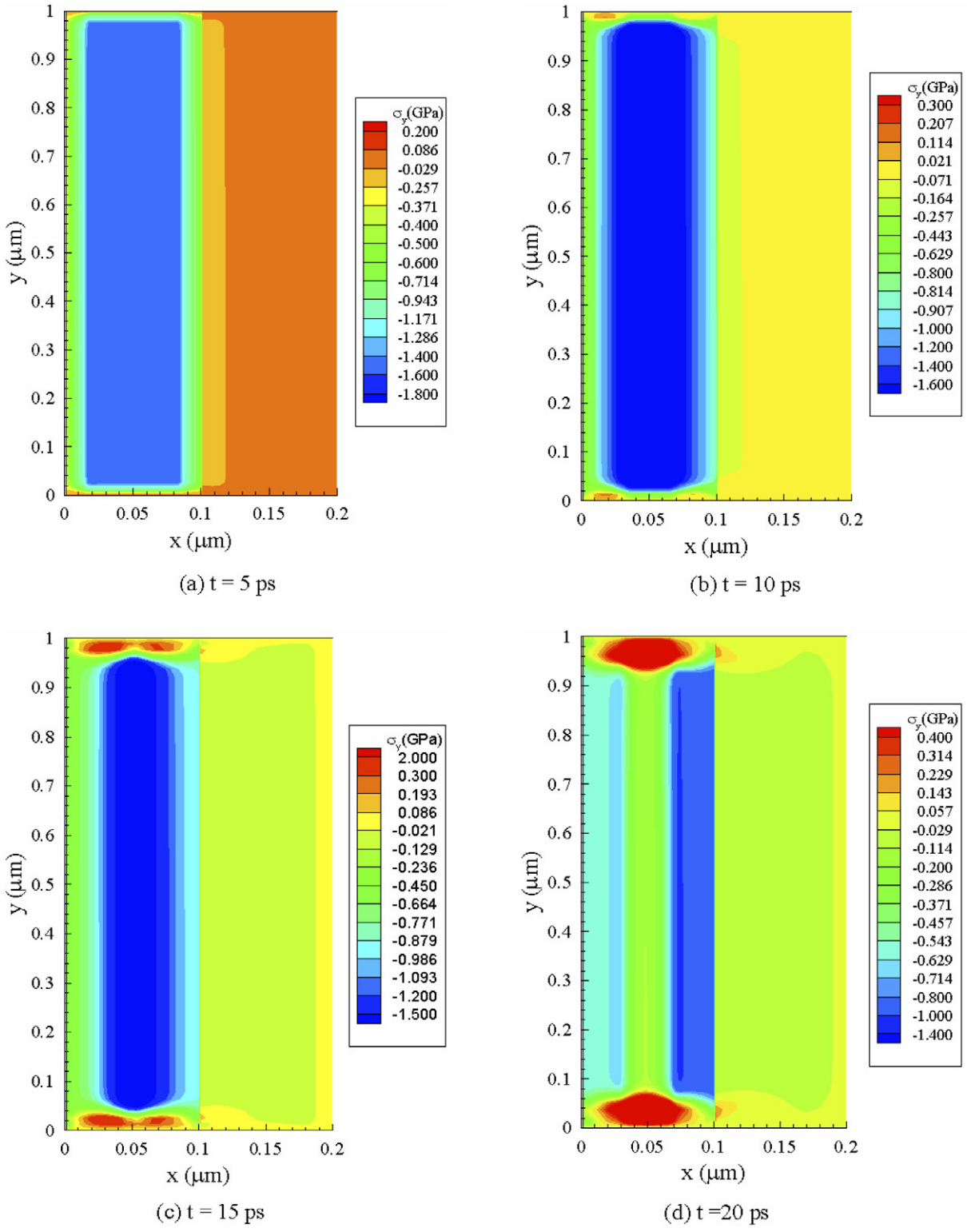

Fig. 15. Normal stress (σ_y) profiles at different times with laser fluence $J = 1000\ \mathrm{J\,m^{-2}}$.

ity of displacement exists at the interface may result in shear failure. Displacement alteration in the gold layer is more pronounced for bonded films with imperfect thermal contact at interface. Numerical results also show there are not non-physical oscillations.

References

[1] D.Y. Tzou, J.K. Chen, J.E. Beraun, Hot-electron blast induced by ultrashort-pulsed lasers in layered media, Int. J. Heat Mass Transfer 45 (2002) 3369–3382.

[2] A. Mandelis, S.B. Peralta, Thermal wave based materials characterization

and nondestructive evaluation of high-temperature superconductors: a critical review, in: R. Kossowsky (Ed.), Physics and Materials Science of High Temperature Superconductors II, Kluwer Academic, Boston, MA, 1992, pp. 413–440.
[3] J. Opsal, The application of thermal wave technology to thickness and grain size of aluminum films, in: Metalization: Performance and Reliability Issues for VLSI and ULSI, SPIE, 1596, 1991, pp. 120–131.
[4] J.A. Knapp, P. Borgesen, R.A. Zuhr, Beam-solid interactions: physical phenomena, Mater. Res. Soc. Symp. Proc. 157 (1990).
[5] D.J. Elliot, B.P. Piwczyk, Single and multiple pulse ablation of polymeric and high density materials with excimer laser radiation at 193 nm and 248 nm, Mater. Res. Soc. Symp. Proc. 129 (1989) 627–636.
[6] C.P. Grigoropoulos, Heat transfer in laser processing of thin films, in: C.L. Tien (Ed.), Annual Review of Heat Transfer, vol. V, Hemisphere, New York, 1994, pp. 77–130.
[7] J. Narayan, V.P. Gosbole, G.W. White, Laser method for synthesis and processing of continuous diamond films on nondiamond substrates, Science 252 (1991) 416–418.
[8] J.M. Hopkins, J. Sibbett, Ultrashort-pulse lasers: big payoffs in a flash, Sci. AM 283 (2000) 72–79.
[9] J. Liu, Preliminary survey on the mechanisms of the wave-like behaviors of heat transfer in living tissues, Forschung im Ingenieurwesen 66 (2000) 1–10.
[10] C. Momma, S. Nolte, B.N. Chichkov, F.V. Alvensleben, A. Tunnermann, Precise laser ablation with ultrashort pulses, Appl. Surf. Sci. 109 (1997) 15–19.
[11] M.D. Shirk, P.A. Molian, A review of ultrashort pulsed laser ablation of materials, J. Laser Appl. 10 (1998) 18–28.
[12] D.Y. Tzou, Ultrafast heat transport: the lagging behavior, in: 44th SPIE's Annual Meeting 1999 July 18–22, Denver, CO.
[13] D.Y. Tzou, Ultrafast Transient Behavior in Microscale Heat/Mass Transport, Advanced Photon Source Millennium Lecture Series, Argonne National Laboratories, Chicago, 2000.
[14] D.Y. Tzou, Microscale heat transfer and fluid flow, in: 45th SPIE's Annual Meeting 2000 July 30–August 4, San Diego, CA.
[15] H. Wang, W. Dai, R. Melnik, A finite difference method for studying thermal deformation in a double-layered thin film exposed to ultrashort-pulsed lasers, Int. J. Thermal Sci. 45 (2006) 1179–1196.
[16] H. Wang, W. Dai, R. Nassar, R. Melnik, A finite difference method for studying thermal deformation in a thin film exposed to ultrashort-pulsed lasers, Int. J. Heat Mass Transfer 49 (2006) 2712–2723.
[17] W.B. Lor, H.S. Chu, Propagation of thermal waves in a composite medium with interface thermal boundary resistance, Numer. Heat Transfer 36 (1999) 681–697.
[18] W.B. Lor, H.S. Chu, Effect of interface thermal resistance on heat transfer in a composite medium using the thermal wave model, Int. J. Heat Mass Transfer 43 (2000) 653–663.
[19] E.T. Swartz, R.O. Pohl, Thermal boundary resistance, Rev. Modern Phys. 61 (1989) 605–668.
[20] S.D. Brorson, J.G. Fujimoto, E.P. Ippen, Femtosecond electron heat transfer dynamics in thin gold films, Phys. Rev. Lett. 59 (1987) 1962–1965.
[21] J.K. Chen, J.E. Beraun, C.L. Tham, Comparison of one-dimensional and two-dimensional axisymmetric approaches to the thermomechanical response caused by ultrashort laser heating, J. Opt. A: Pure Appl. Opt. 4 (2002) 650–661.
[22] T.Q. Qiu, C.L. Tien, Short-pulse laser heating on metals, Int. J. Heat Mass Transfer 35 (1992) 719–726.
[23] S.P. Timoshenko, J.N. Goodier, Theory of Elasticity, third ed., McGraw-Hill, 1970.
[24] G.W.C. Kaye, T.H. Laby, Tables of Physical and Chemical Constants, fifteenth ed., Longman, London, UK, 1993, p. 31.